Enhanced visible-light photocatalytic activity of carbonate-doped anatase TiO$_2$ based on the electron-withdrawing bidentate carboxylate linkage

Juming Liu [a,b], Lu Han [a], Ning An [a], Lei Xing [c,*], Huiyan Ma [a], Lin Cheng [a,*], Jucai Yang [b], Qiancheng Zhang [a,*]

[a] Key Laboratory of Industrial Catalysis of the Inner Mongolia Autonomous Region, Inner Mongolia University of Technology, Huhhot 010051, China
[b] School of Energy and Power Engineering, Inner Mongolia University of Technology, Huhhot 010051, China
[c] School of Chemical Engineering, University of Birmingham, Edgbaston, Birmingham B15 2TT, UK

ARTICLE INFO

ABSTRACT

Carbonate-doped anatase TiO$_2$ photocatalysts were prepared by a conventional sol-gel method and subsequent xerogel carbonization process in hypoxic atmosphere. Acetic acid was used as the hydrolysis inhibitors of titanium butoxide (TBOT) and the carbon source was the organic species produced during the synthesis of TiO$_2$ particles. Via a low-temperature ($\leq$300 °C) carbonization process, the carboxylate ligands from the chelated acetic acid molecules can be retained and transformed into the bidentate carboxylate linkage between the amorphous carbonate dopants and TiO$_2$ lattice. The strong electron-withdrawing bidentate carboxylate ligands can induce valence band (VB) tail states to narrow the bandgap of TiO$_2$, as confirmed by attenuated total reflection Fourier transform infrared (ATR-FTIR) spectroscopy and X-ray photoelectron spectroscopy (XPS) analyses. Moreover, the carbonate dopants can serve as photosensitizer to absorb visible-light and help to promote the charge carriers' separation through cooperation with bulk/surface defects of TiO$_2$. The synergistic effects can significantly enhance the visible-light photocatalytic activities of TiO$_2$ for phenol degradation ($\lambda \geq$ 420 nm). The band structure and possible photocatalytic mechanism of the carbonate-doped TiO$_2$ were thus elucidated.

© 2016 Elsevier B.V. All rights reserved.

1. Introduction

Semiconductor-based photocatalysis has been identified as an effective method to degrade and eliminate harmful organic pollutants from waste water. Although many novel photocatalysts with various performances have been proposed to date, titanium dioxide (TiO$_2$) is still the most promising photocatalyst because of its low cost, nontoxicity, abundance, and high thermal and chemical stabilities [1–6]. TiO$_2$ exists primarily in four polymorphs, anatase, rutile, brookite, and TiO$_2$ (B) [4]. Among these four phases, anatase TiO$_2$ has been commonly reported to show the highest photocatalytic activity. However, due to its bandgap of 3.2 eV, pure anatase TiO$_2$ can absorb photons only in the ultraviolet (UV) region of the solar spectrum that accounts for ca. 3%–5% of the solar energy reaching the Earth's surface [5], limiting its efficiency for light harvesting. In addition, the high recombination rate of the photoinduced electron-hole pairs that reduces the photoefficiency of the photocatalytic process is another major drawback of TiO$_2$ as a photocatalyst [6]. Therefore, extensive efforts have been undertaken to improve the optical response of TiO$_2$ in the visible-light region and restrain the recombination of photoinduced carriers. These have been mainly achieved by introducing either anion or cation dopants (main group elements, transition metals, or rare earth) into the TiO$_2$ lattice [1,5,6].

Recently, increasing interest has been directed to carbonate-doped TiO$_2$ photocatalysts because of their high visible-light photocatalytic activity for degradation of water pollutants as well as production of hydrogen from water [7–12]. It has been demonstrated that in addition to effectively narrowing the TiO$_2$ bandgap [7,8], carbonate doping can also induce visible-light photocatalytic activity in TiO$_2$ by playing the role of photosensitizer [13–16]. To the best of our knowledge, "carbonate" as a specific term can be used to describe a series of oxygen-containing carbon species, such as carbonate anion, carbonyl, carboxyl, ester, and acyl. However, the question of whether all of these oxygen-containing carbon species

can contribute to enhancing the visible-light photocatalytic activity has not been investigated in depth. Moreover, we note that different "carbonates" display different abilities for binding to TiO_2. In particular, carboxyl, which possesses strong covalent binding ability to TiO_2, is often employed to act as the anchoring group for dye-sensitized solar cells [17,18]. Generally, such strong covalent binding may strongly influence the electronic environments for Ti cations and O anions, as well as the energy band structure of TiO_2. However, such structural features and the effect on the photocatalytic activity have not been explored systematically to date.

In the present work, we prepared a series of carbonate-doped TiO_2 photocatalysts using a conventional sol-gel method and subsequent xerogel carbonization process in hypoxic atmosphere under different temperatures. The structures and morphologies of the as-prepared samples were investigated using a variety of characterization techniques. In particular, the structural features of carboxylate ligands and their effects on the band structure of TiO_2 were investigated in detail by attenuated total reflection Fourier transform infrared (ATR-FTIR) spectroscopy and X-Ray photoelectron spectroscopy (XPS) analyses. The photocatalytic activity was evaluated by the photodegradation of phenol under visible-light irradiation ($\lambda \geq 420$ nm). Finally, based on the results of characterization and experiment, the possible band structure and mechanism of the enhanced photocatalytic activity based on the electron-withdrawing bidentate carboxylate linkage were proposed for the carbonate-doped TiO_2.

2. Experimental section

2.1. Photocatalyst preparation

Carbonate-doped TiO_2 was prepared by the conventional sol-gel method followed by the xerogel carbonization process. All chemicals were used as received without further purification. Distilled water was used for the preparation of all aqueous solutions.

Typically, 10 mL glacial acetic acid (AcOH), 20 mL anhydrous ethanol, and 5 mL distilled water were mixed in a 200 mL flask with stirring for 10 min to obtain solution A. Meanwhile, 10 mL titanium butoxide (TBOT, $\geq$99.0%) and 20 mL anhydrous ethanol were mixed with stirring for 10 min to obtain solution B. The solution A was added dropwise into the solution B slowly under vigorous and magnetic stirring of the reaction mixture in order to form the sol. The sol was stirred continuously for 30 min and aged for 48 h to form the gel at room temperature. After that step, the gel was dried for 12 h at 90 °C to obtain the xerogel that was then milled and placed into a ceramic boat. Next, the xerogel was carbonized using a tube furnace at different temperatures with a ramping rate of 5 °C/min and held for 2 h to prepare the carbonate-doped TiO_2. The carbonization was performed in a hypoxic atmosphere (5% O_2, 95% N_2, 100 mL/min), which was beneficial for obtaining a suitable level of carbonate doping. The final products were allowed to cool to room temperature naturally. The carbonate-doped TiO_2 samples were labeled as CT-x, where "x" indicated the carbonization temperature (°C).

2.2. Characterization

X-ray diffraction (XRD) patterns were collected using a PANalytical Empyrean X-ray diffractometer with Cu Kα radiation. Nitrogen adsorption/desorption measurements at 77 K were performed using a Quadrasorb SI-MP apparatus. The surface area was calculated using BET method within the relative pressure (P/P_0) range of 0.05–0.30. Raman spectra were measured by a Renishaw inVia confocal Raman microscope equipped with a 532 nm

green laser source. The morphologies of carbonate-doped TiO_2 was observed by transmission electron microscopy (TEM, FEI Tecnai F20). The sample for TEM measurements was suspended in ethanol and supported onto a holey carbon film on a Cu grid. X-ray photoelectron spectra (XPS) were obtained using a Thermon ESCAlab 250 X-ray photoelectron spectrometer with an Al Kα X-ray source. To investigate the local chemical state of the functional groups on the surface, curve fitting of the raw data of the Ti 2p, O 1s and C 1s spectra was performed using the public software package XPSPEAK v4.1. Ar^+ ion etching at 3 kV for 6 min on a 2 mm × 2 mm sample was used to remove the surface oxide to unveil subsurface information for comparison. Fourier-transform infrared (FTIR) spectroscopy measurements were carried out using a Perkin Elmer Frontier FTIR spectrometer with an attenuated total reflection (ATR) accessory. Ultraviolet visible diffuse reflectance spectra (UV–vis DRS) were recorded in the 300–700 nm range in reference to barium sulphate ($BaSO_4$) using a UV–vis spectrometer (UV-3600, Shimadzu). Photoluminescence (PL) emission spectra was acquired under excitation at 280 nm using an SHIMADZU RF-5301 PC spectrometer.

2.3. Visible-light photocatalytic degradation of phenol

The photocatalytic activity of carbonate-doped TiO_2 was evaluated using phenol degradation in aqueous solution under visible-light irradiation. The light source was a 20 W blue light-emitting diode (LED) lamp. The wavelength of the blue LED was in the range of 410–500 nm. The short wavelength components of the light were cut off using a glass optical filter ($\lambda \geq 420$ nm) (Fig. S1, Supplementary Material). In a typical experiment, 0.1 g of the as-prepared carbonate-doped TiO_2 was added into 30 mL of 20 mg/L phenol solution in a 50 mL quartz beaker. Prior to irradiation, the suspensions were magnetically stirred for 1 h to achieve adsorption-desorption equilibrium for phenol. Then, the suspensions were illuminated with the above-mentioned light source. To determine the change in the phenol concentration in solution during the process, a 3.0 mL solution sample was taken from the reaction mixture every 30 min and subsequently filtered through a millipore filter (pore size 0.22 μm) in order to remove the catalyst. This solution was then analyzed using a UV–vis spectrometer. The phenol concentration was obtained according to the linear relation between the absorbance at 270 nm and the phenol solution concentration [8,19].

2.4. Measurement of evolved CO_2

Photocatalytic evolution of CO_2 was measured in a 50 mL sealed quartz volumetric flask with stirring at ambient temperature using the above-mentioned LED as the light source. In a typical experiment, 0.1 g of CT-300 was dispersed in 30 mL of 20 mg/L phenol solution. Prior to irradiation, the suspensions were magnetically stirred for 1 h to achieve the adsorption-desorption equilibrium for phenol. At regular time intervals during the illumination process, 0.5 mL of the gas in the headspace was withdrawn using a gas-tight syringe and analyzed by a gas chromatograph with a thermal conductivity detector (TCD), equipped with MS-13X packed column. The molar amount of CO_2 was quantified using the external standard method.

2.5. Action spectrum of phenol degradation

The photocatalytic degradation of phenol in the presence of CT-300 was investigated as a function of irradiation wavelength in a 15 mL quartz colorimetric tube with stirring at ambient temperature. In a typical experiment, 16.7 mg of CT-300 was dispersed in 5 mL of 20 mg/L phenol solution. The suspension was stirred in the dark environment for 60 min, to achieve the adsorption-desorption

equilibrium for phenol, and then irradiated for 30 min under stirring. A series of monochromatic 5 W LEDs were employed as the irradiation source (Fig. S2, Supplementary Material). The irradiation intensity was measured using an irradiatometer (FZ-A, Beijing Normal University Optical Instrument, China). The wavelength-dependent apparent quantum efficiency, Φ_{app}, was defined as the rate ratio of the consumption of photogenerated holes and the flux of incident photons, by taking into account the fact that 28 electrons (holes) are required according to the stoichiometry of the following reaction: $C_6H_6O + 7O_2 \rightarrow 6 CO_2 + 3H_2O$.

2.6. Measurement of hydroxyl radicals

The photocatalytic activity of CT-300 was also evaluated by measuring the formation of hydroxyl radicals ($\bullet$OH) in solution. It was analyzed by a photoluminescence (PL) technique using coumarin as a probe molecule, which reacts with $\bullet$OH radicals readily to produce 7-hydroxycoumarin as a highly fluorescent product. In a typical experiment, the 1.0 g/L CT-300 suspension, containing 0.5 mmol/L coumarin and 20 mg/L phenol, was mixed under magnetic stirring, and then shaken overnight. After that, the suspension was illuminated with the above-mentioned LED light source. At given intervals, small aliquots were withdrawn by a syringe, and filtered through a millipore filter (pore size 0.22 μm) in order to remove the catalyst. The filtrate was then analyzed using a SHIMADZU RF-5301 PC fluorescence spectrophotometer by the excitation at the wavelength of 332 nm.

3. Results and discussions

3.1. Morphology and structure

Fig. 1 shows the digital photographs of the carbonate-doped TiO$_2$ samples. With the increased carbonization temperature, the visible color of the resulting powders changes from light yellow for CT-100 and CT-200, dark brown for CT-300, earthy yellow for CT-400, to light grey for CT-500, with all of these samples showing a striking contrast to the white color of the pristine anatase TiO$_2$. These results indicate that the surface properties of TiO$_2$ are apparently affected by the xerogel carbonization process in a hypoxic atmosphere at different temperatures.

The XRD patterns of the as-prepared carbonate-doped TiO$_2$ samples are presented in Fig. 2(a). All diffraction peaks can be assigned to those of the tetragonal anatase phase (JCPDS 99-0008). Diffraction peaks due to other polymorphs of TiO$_2$ such as rutile and brookite are absent. The TiO$_2$ crystallinity increases with the carbonization temperature. For CT-100, CT-200 and CT-300, the diffraction peaks show weak intensity and significantly broadened full width half maximum (FWHM), which can be attributed to the poor crystallinity and very small size of the TiO$_2$ crystallites. With the higher carbonization temperature, the diffraction peaks' intensities increase abruptly for CT-400 and CT-500, indicating a better crystallinity and fewer crystal defects. The crystallite sizes of carbonate-doped TiO$_2$ from CT-100 to CT-500 were estimated using the Scherrer's equation and are given in Table 1. It can be observed that the nanocrystallite size increases with the carbonization temperature. However, the increment of the crystalline size was relatively small, which can be attributed to the stabilizing effects of AcOH on the precursors that could restrain the crystallization process of TiO$_2$ [20–22]. It is well known that the smaller crystalline size the larger specific surface area, the BET surface areas of the as-prepared carbonate-doped TiO$_2$ samples were therefore calculated according to the nitrogen adsorption-desorption isotherms (Fig. S3, Supplementary Material) and summarized in Table 1. It can be seen that the samples prepared at lower tempera-

tures (CT-100, CT-200 and CT-300) show relatively high BET surface area. When the carbonization temperature further increases to 400 or 500 °C (CT-400 or CT-500), the BET surface area decreases markedly, which should be related to the larger crystalline size at higher temperature.

Fig. 2(b) presents the Raman spectra of the as-prepared carbonate-doped TiO$_2$ samples in the 800–100 cm^{-1} range in order to investigate the formation of TiO$_2$. All samples show the peaks at ca. 638 cm^{-1} (E_g), 516 cm^{-1} (A_{1g}), 395 cm^{-1} (B_{1g}), 200 cm^{-1} (E_g), and 150 cm^{-1} (E_g), indicating the existence of a predominant anatase phase in these samples [23,24]. Close inspection of the strongest and sharpest peak at ca. 150 cm^{-1} reveals a red shift towards the lower frequency for higher carbonization temperature from 100 to 500 °C, indicating the reduction of surface defects due to the temperature processing and crystal growth [24]. Together with the results from XRD, these results indicated that it is reasonable to conclude that the carbonate-doped TiO$_2$ samples prepared at lower temperature ($\leq$300 °C) contains more bulk and/or surface defects.

The crystal structure and morphology of the carbonate-doped TiO$_2$ samples are examined by high-resolution transmission electron microscopy (HRTEM). Fig. 3 shows the HRTEM images and the results of fast Fourier transform (FFT) analyses of CT-300. As shown in Figs. 3(a) and S4 (Supplementary Material), the carbonate-doped TiO$_2$ particles are comprised of a large number of nanocrystallites, which abut against each other within the particles. The crystallite size determined from the HRTEM image is ca. 10 nm, consistent with the crystallite size extracted from the width of the XRD patterns. Lattice fringes with an interplanar spacing of 0.35 nm are clearly observed and are consistent with spacing between the (101) planes of tetragonal anatase, in good agreement with the results of XRD and Raman. To determine the local structural features, a selected area of the image is filtered using FFT as shown in Fig. 3(b). The FFT pattern of the selected area shows both the spots pattern for crystalline phase and the diffusing ring pattern for the amorphous phase. After applying band pass mask tools to the spots and diffuse ring, the corresponding Fourier-filtered images are obtained by further inverse FFT operation, as shown in Fig. 3(c) and (d). The Fourier-filtered image of the spots pattern (Fig. 3(c)) clearly shows severe lattice distortions, with several developing into dislocations in the selected area, confirming the existence of bulk and/or surface defects. Meanwhile, the Fourier-filtered image of the diffuse ring pattern shows that the amorphous phase is evenly distributed in TiO$_2$ lattice. Because no apparent peaks for graphite-like carbon were observed in Raman analysis (Fig. S5, Supplementary Material) [24,25], such amorphous phase should be attributed to the carbonate dopants in TiO$_2$, as discussed in the next section.

3.2. Surface chemical analysis

To investigate the chemical states of the carbonate dopants, XPS was used to record the C 1s high resolution spectra for all samples, as shown in Fig. 4(a). The major peak at 284.5 eV can be attributed to the C—C neutral bond, for which the high intensity is an indicator of the carbonate species doped into TiO$_2$ rather than external hydrocarbon contaminations [26–29]. The peaks centered at 285.9 eV and 288.5 eV match the XPS peaks of C—OR(H) and C—OOR(H), respectively, confirming that all five samples were successfully doped by carbonate species [7,10,26–30]. In addition, the absence of the peak at 282.0 eV indicates that the carbon species do not substitute oxygen species in the TiO$_2$ lattice to form a C—Ti bond [7,11,24]. Therefore, it is very likely that the amorphous carbonate dopants are mainly located at the interstitial and/or surface position of the TiO$_2$ lattice [31].

Apparently, C 1s XPS spectra could not provide us more information to identify the binding mode between the carbonate dopants
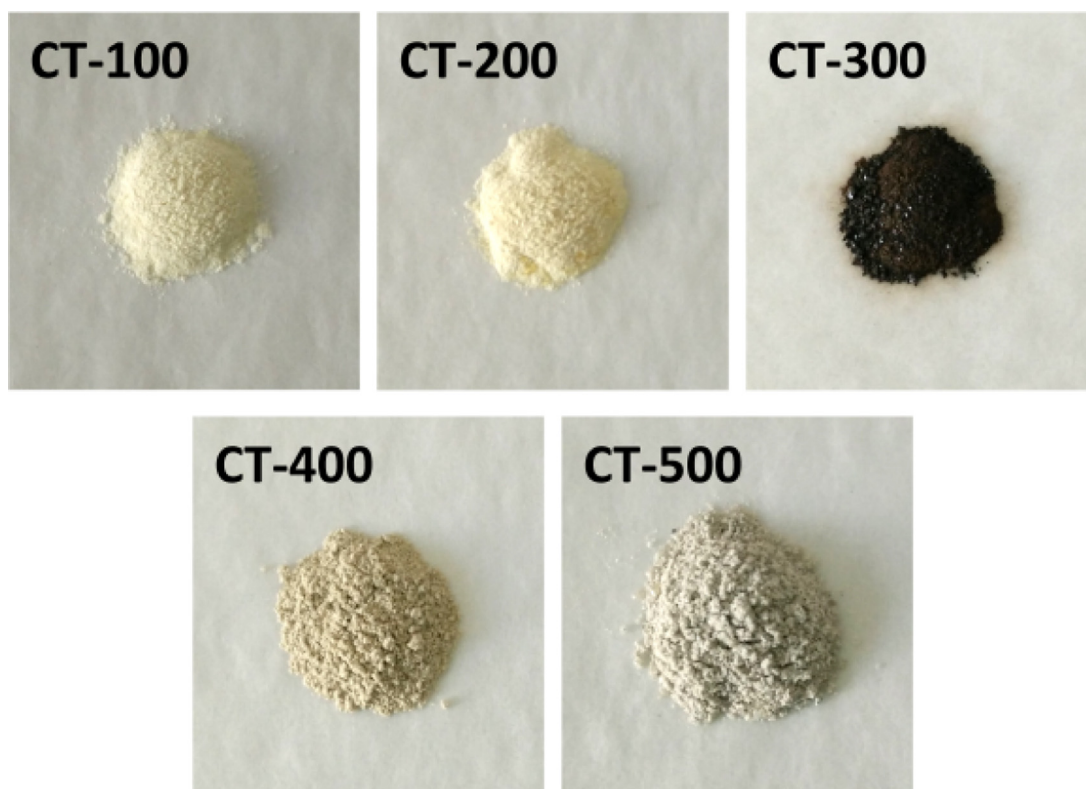
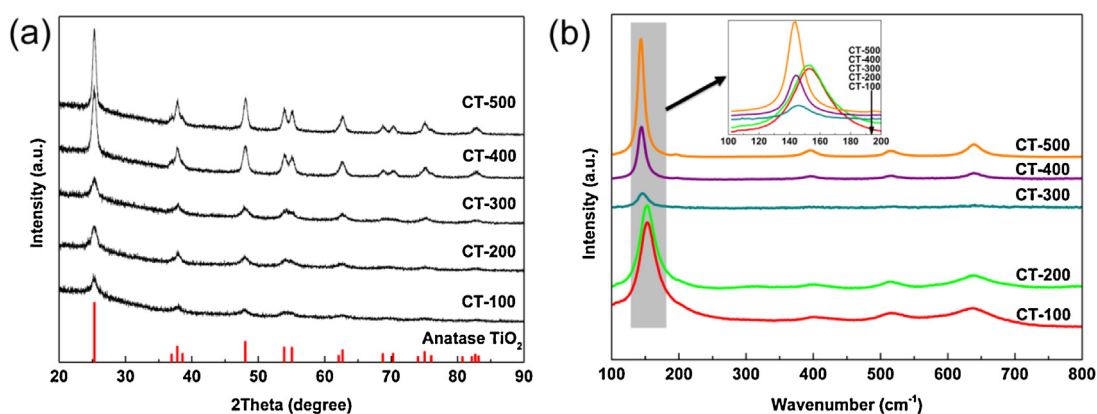**Fig 1.** Photographs of carbonate-doped TiO_2 synthesized at 100–500 °C.

Fig. 2. (a) XRD patterns and (b) Raman spectra of carbonate-doped TiO_2 synthesized at 100–500 °C in the 1000–2000 cm^{-1} range. An expanded part of the Raman spectra in the range of 200–100 cm^{-1} is shown in the inset.

and TiO_2, hence ATR-FTIR analysis was carried out for all samples. The total reflection capabilities of ATR-FTIR allow the wave to propagate along the region near the carbonate dopants/TiO_2 interface, enhancing the carbonate species signal [18]. As shown in Fig. 4(b), the peaks observed at ca. 1526 cm^{-1} and 1445 cm^{-1} can be attributed to the antisymmetric and symmetric stretching

Table 1
Carbonization temperature, crystallite size, BET surface area and surface element content of the carbonate-doped TiO_2 samples.

Sample	Carbonization temperature (°C)	Crystallite size (nm)	BET surface area ($m^2 g^{-1}$)	Surface element content (at.%)[a]		
				Ti	O	C
CT-100	100	10.0	271.6	4.75	26.58	68.67
CT-200	200	10.7	283.9	10.55	41.13	48.32
CT-300	300	10.1	255.9	17.06	48.77	34.17
CT-400	400	13.3	116.3	18.39	48.27	33.34
CT-500	500	14.3	61.5	21.28	53.18	25.54

[a] Surface element content for every sample was calculated from the corresponding XPS survey spectra.
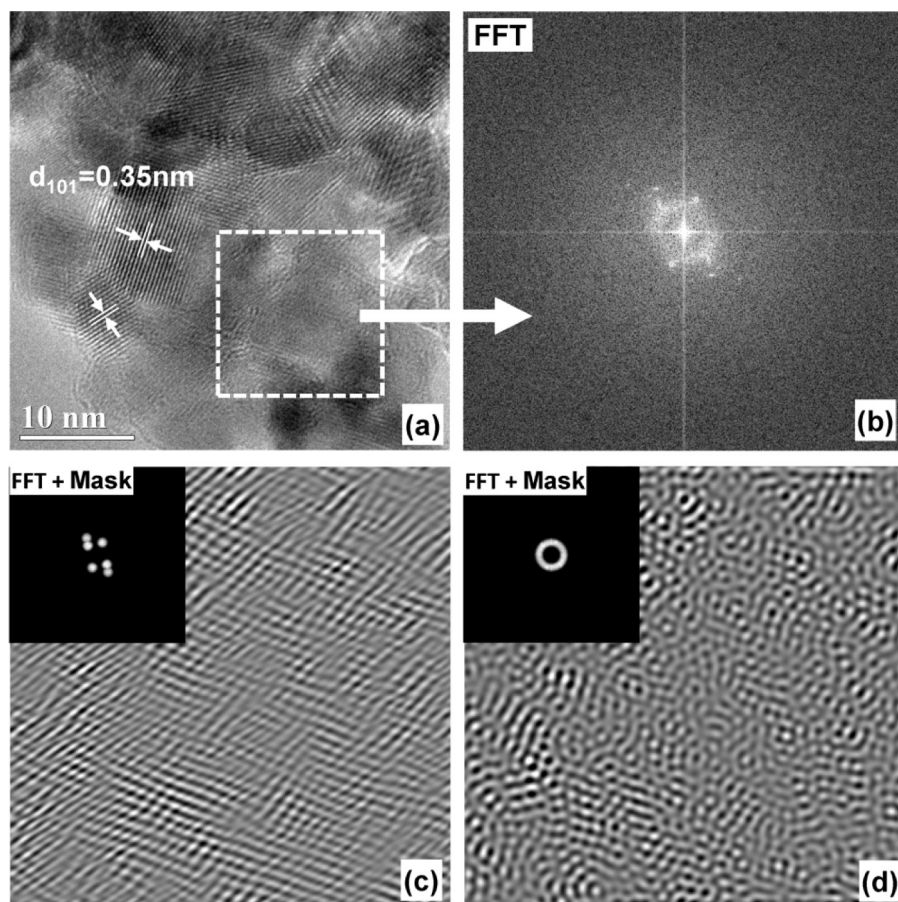
Fig. 3. (a) HRTEM image of carbonate-doped TiO_2 synthesized at 300 °C. (b) FFT pattern of the selected area. (c) Application of band-pass masking tool to the spot of FFT pattern (shown as inset) and the corresponding inverse FFT image. (d) Application of band-pass masking tool to the diffuse ring of FFT pattern (shown as inset) and the corresponding inverse FFT image.

vibration of the coordinated carboxylate ligands on TiO_2 [32,33]. In our preparation, AcOH was employed to suppress the rapid hydrolysis and condensation of TBOT via the chelation of AcOH molecules to the Ti cations. Carboxyl groups show a strong binding ability to the Ti cations [34]. These coordinated carboxylate ligands are most likely derived from the chelated AcOH molecules under lower carbonization temperatures. When the carbonization temperature is increased from 100 to 200 °C, the intensities of carboxylate peaks decrease slightly, indicating a slight decomposing of the carboxylate chelate structure. On the other hand, at 300 °C, the intensity of carboxylate peaks decreases abruptly, indicating an intense decomposition of the carboxylate ligands due to a more aggressive carbonization. With the higher carbonization temperature (400 and 500 °C), these characteristic peaks eventually fade away in samples CT-400 and CT-500, possibly due to the total breakdown of carboxylate chelate structure under high temperatures. Therefore, it is only when the carbonization temperature is sufficiently low ($\leq$300 °C) that the carboxylate ligands can be retained and transformed into a part of carbonate dopants and can coordinate with TiO_2 in final products.

Furthermore, FTIR spectroscopy is also a reliable tool to determine the coordination mode of the carboxylate ligands. Generally, the frequency difference between the antisymmetric and symmetric stretching vibration ($\Delta = \nu_{as} - \nu_a$) has been related to the type of carboxylate coordination. Three possible binding modes have been previously proposed for the coordination of carboxylate ligands on metal oxides: the monodentate (esterlike) linkage ($\Delta = 350–500\,cm^{-1}$), bidentate bridging ($\Delta = 150–180\,cm^{-1}$), and the bidentate chelating ($\Delta = 60–100\,cm^{-1}$) [32,35]. In our study,

the Δ value of the two peaks ($\Delta = 81\,cm^{-1}$) suggests that the binding mode of the carboxylate on TiO_2 is predominantly that of the bidentate chelating linkage (inset in Fig. 4(b)) rather than other two binding modes. With the exception of the double peaks of bidentate carboxylate ligand, the peaks at ca. $1416\,cm^{-1}$ match the symmetric stretching vibration of carboxyl group ($-COOH$) well [36,37], while the shoulder peaks at ca.$1343\,cm^{-1}$ correspond to the deformation vibration of the methyl group ($-CH_3$) [36,38]. These peaks can be attributed to the residual AcOH under lower carbonization temperatures. The broad absorption band at ca. $1634\,cm^{-1}$ for CT-400 and CT-500 can be ascribed to the stretching vibration of surface water or hydroxyl groups [39,40].

The bidentate structure of carboxylate ligands significantly affects the electronic environments for Ti cations and O anions, with these influences recorded by the high resolution XPS spectra of Ti 2p and O 1s regions, as shown in Fig. 4(c) and (d). The surface element content was also calculated according to the XPS survey spectra and is summarized in Table 1. It is clear that the intensities of all Ti 2p and O 1s peaks are enhanced gradually with the increasing temperature, which can be attributed to the decrease of the surface carbon contents (Table 1). In general, the peaks at 457.8–459.6 eV can be assigned to the Ti 2p3/2 binding energy regions, and the peaks at 463.9–464.3 eV can be ascribed to the Ti 2p1/2 binding energy regions, respectively (Fig. 4(c)) [24,29,40]. Interestingly, careful examination reveals that the Ti 2p3/2 peaks for CT-100, CT-200 and CT-300 can be further deconvolved into two components: one at 458.2–458.5 eV and the other at 459.2–459.6 eV, indicating two different types of electronic environments for Ti cations. Gen-
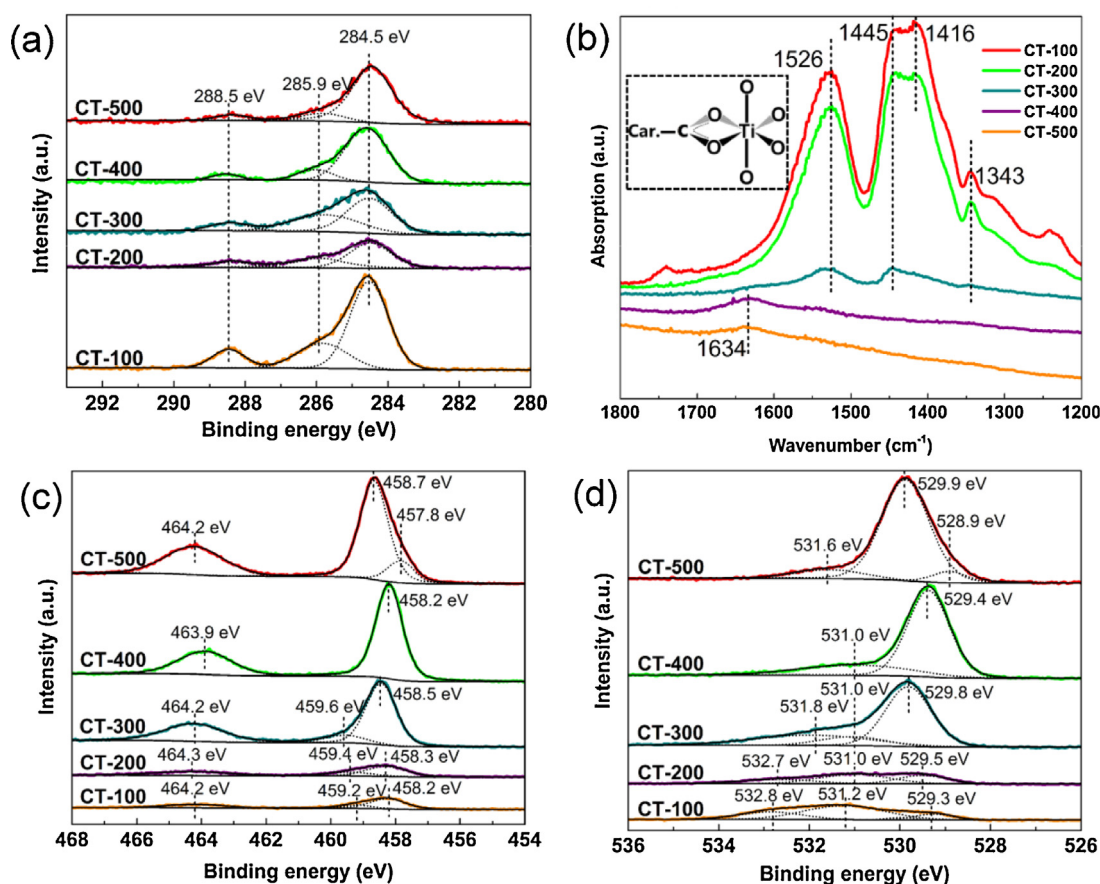
Fig. 4. (a) C 1s, (c) Ti 2p and (d) O 1s high resolution XPS spectra with constituent fitting and (b) ATR-FTIR spectra for carbonate-doped TiO_2 synthesized at 100–500 °C.

erally, a chemical shift to lower binding energy translates into an increased local electron density, while the opposite is true for a shift to higher binding energy [41]. Considering the bidentate carboxylate chelating structure revealed by the ATR-FTIR spectra and the strong electron-withdrawing property of the carboxylate ligand [18,42–45], it is reasonable that the split of Ti 2p3/2 peak is caused by the coordination of carboxylate ligands on the Ti cations. In the present situation, the electron density around the Ti cation coordinated with bidentate carboxylate would be decreased due to the electron-withdrawing character of carboxylate ligands, leading to the increase in the binding energy of Ti 2p, corresponding to Ti 2p3/2 peaks at 459.2–459.6 eV. By contrast, in the absence of the coordinating carboxylate ligands, the electron density around the Ti cation is not affected, and the corresponding Ti 2p3/2 peaks would appear at a lower binding energy (458.2–458.5 eV), similar to the typical value of pristine anatase TiO_2. Moreover, we note that the two split Ti 2p3/2 peaks shift simultaneously towards higher binding energy with increasing carbonization temperature, which can be explained by the decrease of surface organic carbon species. Previous results have shown that the bonding of some organic species or carbon species on the surface of TiO_2 would lead to the shift of Ti 2p3/2 peak toward lower binding energy [41,46–48].

For CT-400, two intense peaks at 458.2 and 463.9 eV are observed, corresponding to the Ti 2p3/2 and Ti 2p1/2 binding energy regions, respectively, indicating the presence of Ti^{4+} ions in TiO_2. We note that the two Ti 2p peaks of CT-400 exhibit a slight shift to a lower binding energy (ca. 0.3 eV) compared to CT-300, which can be attributed to the absence of the electron-withdrawing bidentate carboxylate ligands. When the carbonization temperature reaches 500 °C, in addition to the intense peaks at 458.7 (Ti 2p3/2) and 464.2 eV (Ti 2p1/2), a new peak located at 457.8 eV is

observed that can be assigned to Ti^{3+} ions and oxygen vacancy [29,49]. In fact, CT-500 was prepared in a hypoxic atmosphere under higher carbonization temperature, hence, it should have more oxygen vacancies, and the appearance of Ti^{3+} ions should be normal. Compared to CT-400, the two Ti 2p peaks of CT-500 exhibit a slight shift to higher binding energy (ca. 0.3 eV for Ti 2p1/2 and ca. 0.5 eV for Ti 2p3/2), which is related to the presence of the oxygen vacancies in CT-500 [40].

The high resolution XPS spectra of the O 1s regions are shown in Fig. 4(d). For all five samples, the peaks at 529.3–529.9 eV are related to the O^{2-} anions of the TiO_2 crystalline network [26,27,30,50,51], and the peaks at 531.0–531.6 eV can be attributed to the surface hydroxyl group [26,51–53] or C=O from carbonate dopants [24,27,31,50]. For CT-100 and CT-200, the peaks at 532.7–532.8 eV can be attributed to several contributions from the OH groups of the residual carboxyl groups, H_2O from the TiO_2 surface, and/or from the small amount of organic carbon species [47,54]. However, for CT-300, these peaks (532.7–532.8 eV) fade away and a new peak located at 531.8 eV is observed that can be assigned to the bidentate carboxylate ligand. Finally, this bidentate carboxylate peak disappears in CT-400 due to high temperature, very consistent with the results of FTIR and Ti 2p XPS. In the absence of a bidentate carboxylate ligand, the Ti-O (lattice O) peak of CT-400 exhibits a slight shift to lower binding energy (ca. 0.4 eV) relative to that in CT-300, reconfirming the influence of electron-withdrawing bidentate carboxylate ligands on the electronic environments for the Ti cations and O anions. For CT-500, a new peak located at 528.9 eV is observed, accompanied by a shift of the other two peaks to higher energy that can be related to the Ti^{3+} and oxygen vacancy [40,55]. To investigate the subsurface properties of the carbonate-doped TiO_2 samples, the high resolution XPS analyses after Ar^+
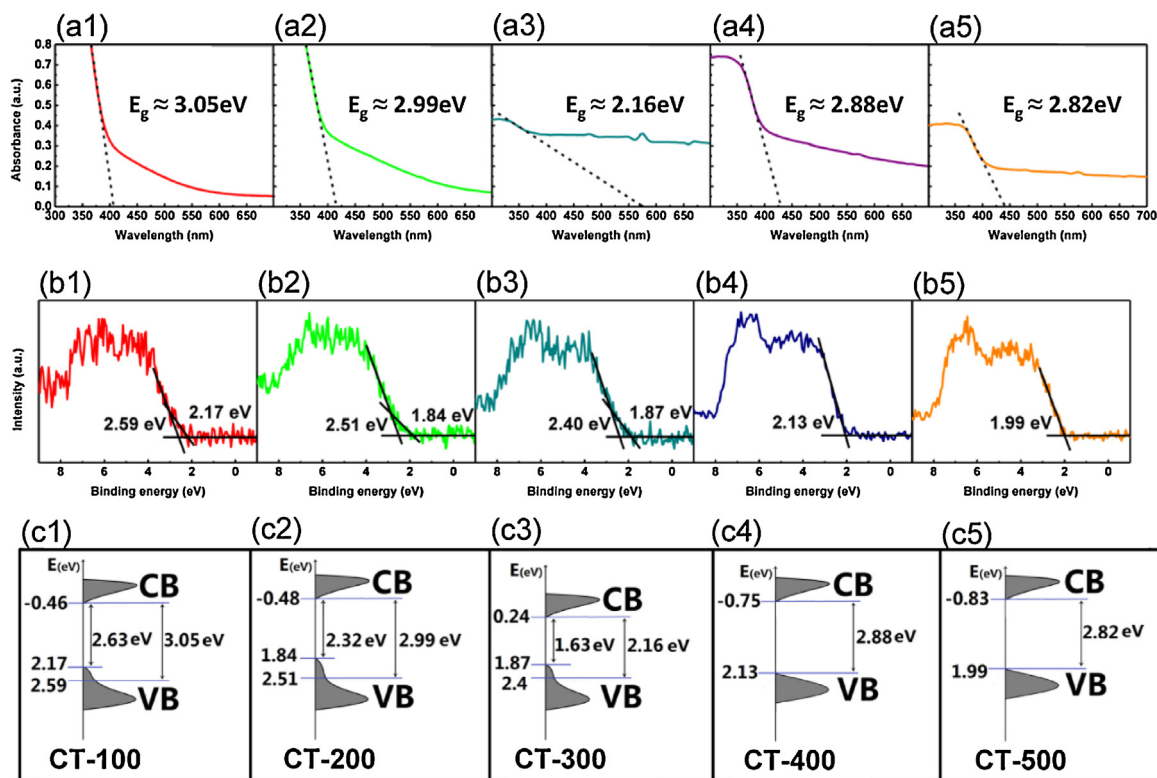
Fig. 5. UV–vis diffuse reflectance spectra ((a1)–(a5)), valence band XPS spectra ((b1)–(b5)) and proposed schematic energy band structure ((c1)–(c5)) of carbonate-doped TiO₂ synthesized at 100–500 °C.

etching were also performed for C 1s, Ti 2p and O 1s regions (details can be found in Supplementary Material, Fig. S6).

In support of the results from ATR-FTIR and XPS analyses, we can conclude that the bidentate carboxylate linkage between the amorphous carbonate dopants and TiO₂ lattice can be obtained under a lower carbonization temperature ($\leq$300 °C) and a hypoxic atmosphere where AcOH is employed as the chelating agent and carbon precursor. Due to the strong electron-withdrawing character of the carboxylate ligands, the electronic environments for Ti cations and O anions are significantly affected. It can be expected that the energy band structure of TiO₂ will also be changed.

3.3. Energy band structure analysis

As shown in Fig. 5, the energy band structure of the as-prepared carbonate-doped TiO₂ was investigated in detail by UV–vis DRS and valence band XPS (VB-XPS). Fig. 5(a1)–(a5) show the UV–vis DR spectra of all five samples from CT-100 to CT-500, respectively. It is found that the spectra of all samples shift to longer wavelengths, revealing the decrease in the bandgap. The bandgap narrowing can be attributed to the doping of various carbonate species [7,31]. In particular, CT-300 shows the maximum optical absorption threshold at ca. 575 nm (red shift) compared to other samples, corresponding to the narrowest bandgap energy of 2.16 eV. Compared to CT-300, other samples exhibit wider bandgaps. It is clearly determined that the bandgaps of all five samples discussed here satisfy the sequence of CT-300 < CT-500 < CT-400 < CT-200 < CT-100. The red shift in the absorption spectrum is also consistent with the change in the color of the samples. It is highly likely that both the carbonization degree and the content of the carbonate dopants can simultaneously affect the bandgap of TiO₂. Due to the lower temperature, the carbonate precursors in CT-100 and CT-200 are not carbonized sufficiently, leading to more organic precursor residuals and poor bandgap narrowing. Nevertheless, CT-400 and

CT-500 also do not achieve the desired bandgap narrowing due to their lower content of carbonate dopants, even though these two samples were carbonized adequately at higher temperatures. Moreover, the overall visible-light absorbances of all five samples are enhanced in varying degrees, with different absorption tails extending up to 700 nm. Previous studies have shown that the carbonate species on the surface of TiO₂ can play the role of photosensitizer with an extended absorption band tail in the visible-light region that is responsible for the enhancement of visible-light absorbance [13–16,56]. The observed "tail-like" features in the UV–vis DR spectra are directly related to the modification of the electronic states due to the carbonate dopants. The optical transitions between these dopants and dopant-induced levels and Ti 3d orbitals can explain the observed visible-light absorptions (from around 450 nm to 700 nm) of these carbonate-doped TiO₂ samples [57].

The total density of states (DOS) of the valence band of carbonate-doped TiO₂ was also measured by VB-XPS, as shown in Fig. 5(b1)–(b5). For the VB-XP spectra of CT-100, CT-200 and CT-300, a notable difference compared with CT-400 and CT-500 is the presence of VB tail states. Combined with the results of XPS and ATR-FTIR, such band tail should be attributed to the strong electron-withdrawing bidentate carboxylate ligands that induces additional diffusive electronic states above the VB edge and causes further bandgap narrowing. Such VB tail states are not observed for CT-400 and CT-500, which can be explained by the thermal decomposition of bidentate carboxylate ligands at high carbonization temperature. In addition, from CT-100 to CT-500, the main VB edge shifts substantially towards the vacuum level (negative shift) and becomes closer to the typical value for the pure anatase TiO₂ (2.01 eV) [58], indicating the decrease in content of the carbonate dopants and lattice defects due to high temperature.

Fig. 5(c1)–(c5) present schematic illustrations of the resolved band structures of the five samples, constructed using the exper-
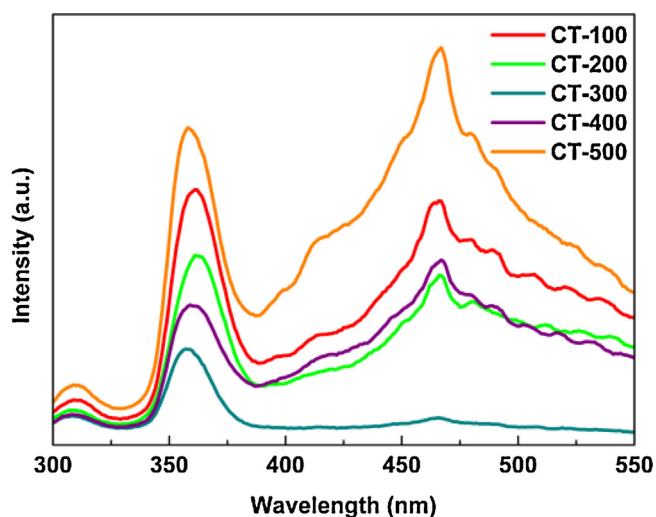
Fig. 6. Photoluminescence spectra of carbonate-doped TiO_2 synthesized at 100–500 °C with the excitation wavelength at 280 nm.

imental data of the UV–vis DRS and the VB-XPS results [8,59]. As shown in Fig. 5(c1)–(c3), according to the VB-XP spectra, the main absorption onsets in CT-100, CT-200 and CT-300 are located at ca. 2.59 eV, 2.51 eV and 2.40 eV, respectively, whereas the valence band maximum (VBM) energies associated with the band tails are located at ca. 2.17 eV, 1.84 eV and 1.87 eV, respectively. Because the bandgaps of the three samples are measured to be ca. 3.05 eV for CT-100, 2.99 eV for CT-200 and 2.16 eV for CT-300 from the UV–vis DR spectra, their corresponding conduction band minimum (CBM) would occur at ca. −0.46 eV, −0.48 eV and 0.24 eV, respectively. Consequently, the remarkable bandgap narrowing of the carbonate-doped TiO_2 with bidentate carboxylate ligands (2.63 eV, 2.32 eV and 1.63 eV) is caused by the substantial shifts of the VB tails. The VBM energies of CT-400 and CT-500 are located at ca. 2.13 eV and 1.99 eV, respectively, as indicated in the VB-XP spectra. UV–vis DR spectra demonstrate that the bandgaps of the two samples are ca. 2.88 eV and 2.82 eV, respectively. Therefore, their corresponding CBM should be located at ca. −0.75 eV and −0.83 eV, respectively. Due to the absence of the VB tail states, the bandgaps of CT-400 and CT-500 are not narrowed further (Fig. 5(c4) and (c5)). Based on the above analyses and considering the bandgap narrowing effect of VB tails, the new bandgap increase in the following order: CT-300 < CT-200 < CT-100 < CT-500 < CT-400.

3.4. PL spectra analysis

Photoluminescence (PL) emission spectra have been frequently used to investigate the efficiency of charge carrier trapping, migration, and transfer in order to understand the fate of electron-hole pairs in semiconductor particles because PL emission results from the recombination of free carriers [60–62]. As shown in Fig. 6, PL spectra are examined at the excitation wavelengths of 280 nm and show peaks at different wavelengths that indicate the trap sites present on the surface of the photocatalyst. According to the results of XPS and UV–vis DRS, high-energy peaks can be assigned to the edge luminescence of the TiO_2 particles, while lower energy peaks are introduced by the presence of the carbonate dopants [63]. The PL spectra show the change in the peak intensity of the five as-prepared samples, increasing in the following sequence: CT-300 < CT-400 < CT-200 < CT-100 < CT-500. The minimum intensity is found for CT-300. The lowest PL intensity of CT-300 indicates the effective inhibition of the recombination of electrons and holes that can likely explained as follows. First, the reduced PL intensity can be explained by the carbonate dopants that can suppress the

electron-hole recombination [10,62]. Another reason may be the existence of appropriate bulk/surface defects upon carbonate doping that can promote the separation of the charge carriers [64]. The intensities of PL signals of CT-100 and CT-200 are higher than that of CT-300, which may be attributed to the excess bulk/surface defects due to the lower carbonization temperatures, as discussed above for the XRD and Raman results. The excess surface defects may act as the centers for the recombination of electrons and holes [64,65]. Moreover, CT-400 and CT-500 also exhibit higher PL intensities than CT-300, which may be related to the significant decrease of carbonate dopants and bulk/surface defects due to the higher carbonization temperatures (as is evident from the ATR-FTIR, XRD and Raman data). Therefore, the separation of charge carriers can be improved more effectively only when the amount of the carbonate dopants and bulk/surface defects is kept at an appropriate level.

3.5. Photocatalytic activities under visible light

Phenol photocatalytic degradation experiments were performed to investigate the photocatalytic activity of the as-prepared carbonate-doped TiO_2 under visible-light illumination ($\lambda \geq 420$ nm). Fig. 7(a) shows the changes in the relative concentrations of phenol in the dark environment and with a certain period of visible-light irradiation. The adsorption-desorption equilibrium of phenol in the dark environment was established within 60 min. In this stage, all five samples do not show any obvious phenol adsorption in water. The large amount of organic carbon residues in CT-100 and CT-200 even leads to a slight increase in absorbance.

In the subsequent photodegradation process, CT-300 shows the highest photocatalytic activity compared to the other samples. After irradiation for 90 min, nearly 90% of phenol is degraded. During the photocatalytic reaction process, the representative UV absorbance spectra of phenol in water are recorded as a function of reaction times in Fig. 7(b). While the degradation of phenol occurs, the evolved CO_2 is simultaneously analyzed using a gas chromatograph equipped with a thermal conductivity detector (TCD), as shown in Fig. 7(c). After irradiation for 180 min, the final amount of CO_2 in gas-phase is around 0.025 mmol, confirming the high degradation efficiency for phenol. It is because, about 0.0064 mmol of phenol (20 mg/L phenol solution, 30 mL) was used for the photocatalytic degradation in this study. If such amount of phenol is completely degraded, the emission of CO_2 would be 0.038 mmol. Consequently, the practical photodegradation efficiency seems to be 66%. However, it is noteworthy that the dissolution of CO_2 in aqueous solution is not considered in the above calculation. In our experiment, when the photodegraded phenol suspension was statically placed in dark environment for 60 min, only 0.0068 mmol of CO_2 in gas-phase was remained, which implies that about 73% of CO_2 in gas-phase was re-dissolved in aqueous solution. Therefore, the practical photodegradation efficiency should be much higher than 66%.

The obvious advantage of CT-300 for the photodegradation of phenol should be attributed to its narrowest bandgap energy and lowest recombination rate of electrons and holes, resulting in a high efficiency of light-harvesting. Moreover, we note that the carbonate dopants on the TiO_2 surface can serve as a photosensitizer for the absorption of visible light and inject electrons into the conduction band of TiO_2. Combined with the results obtained by UV–vis DRS, these results mean that it is very likely that the photocatalytic activity of CT-300 is further promoted via such a photosensitization approach. Therefore, it is reasonable to deduce that the bandgap narrowing, restraint of electron-hole recombination and photosensitization of surface carbonate dopants may synergistically contribute to the enhanced photocatalytic activity
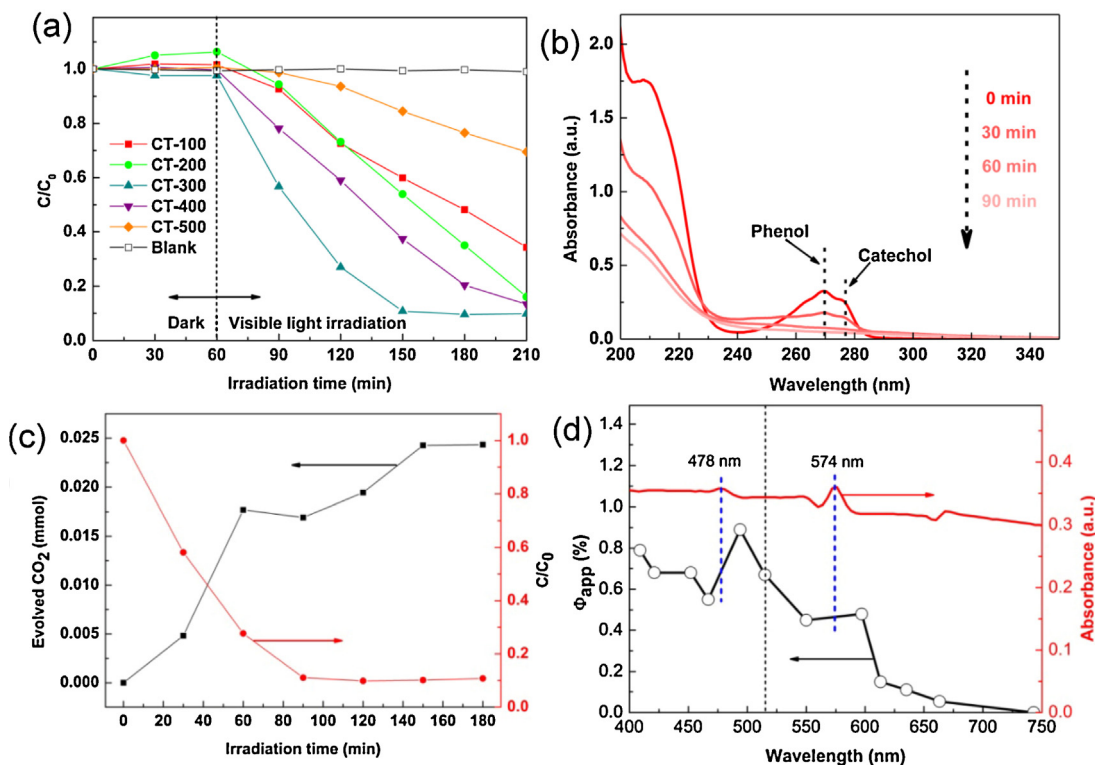
Fig. 7. (a) Photocatalytic degradation of phenol in the presence of carbonate-doped TiO_2 synthesized at 100–500 °C under visible light irradiation ($\lambda \geq 420$ nm). (b) Representative UV–vis absorbance spectra of phenol in water as a function of reaction times using CT-300 as the photocatalyst. (c) Photocatalytic degradation of phenol and evolved CO_2 in the presence of CT-300 under visible light irradiation ($\lambda \geq 420$ nm). (d) Action spectrum of phenol degradation and absorption spectrum of CT-300.

of CT-300. The CT-300 photocatalyst is also very stable and can be recycled several times, as shown in Fig. S7.

In order to elucidate the photoresponse performance of CT-300 in visible-light region, the photocatalytic degradation of phenol was also investigated systematically as a function of irradiation wavelength, by collecting the so-called action spectrum [66,67]. The obtained action spectrum and absorption spectrum of CT-300 are compared in Fig. 7(d). The most straightforward demonstration that a certain material is an effective photocatalyst consists in the resemblance of its action spectrum with its absorption spectrum [66]. It can be seen that the action and absorption spectrum of CT-300 coincide in their peak positions of ca. 478 nm and 574 nm, which partially demonstrates the resemblance. In the 400–515 nm wavelength range, the apparent quantum efficiency does not show any significant decline, and the related absorption spectrum exhibit exactly the similar trend, indicating that CT-300 is an effective photocatalyst for phenol degradation in this region. However, in the 515–750 nm wavelength range, the apparent quantum efficiency decreases gradually with the wavelength, whereas the corresponding absorption spectrum does not show any appreciable decline, indicating an increase in ineffective visible-light absorption that cannot induce any appreciable activity for phenol photocatalytic degradation in this irradiation wavelength range. This result may be rationalized by considering the following reasons:

1) The decreased photon energy would lead to the drop of the oxidative power of the photoinduced holes, until finally the photoinduced holes cannot effectively oxidize the adsorbed H_2O to produce the •OH radical.
2) For the photosensitization approach, the oxidized photosensitizer needs to be reduced again, e.g. by oxidation of phenol or other possible intermediates [13]. With the increased wavelength, the oxidized photosensitizer might lack enough

oxidative power to trigger the subsequent redox process, due to the decreased photon energy.

Although CT-400 possesses the widest bandgap among all five samples, it unexpectedly exhibits a high photocatalytic activity with 87% degradation efficiency in 150 min, which is lower than that of CT-300 but higher than those of the other samples. As discussed in our previous report [31], without considering its lower charge carrier recombination rate, the photosensitization of the surface carbonate dopants may be an important reason for the relatively high photocatalytic activity of CT-400. Due to the poor crystallinity, too many bulk/surface defects and higher charge carrier recombination rate, CT-100 and CT-200 show lower photocatalytic activities than CT-300 and CT-400. The excessive recombination of charge carriers and the lowest content of carbonate dopants can be responsible for the worst photocatalytic activity shown by CT-500.

3.6. Mechanisms of the enhanced photocatalytic activity

As shown in Fig. 8, two possible mechanisms of the enhanced visible-light photocatalytic activity of CT-300 are proposed on the basis of the characterization results described above. There are two possible pathways for the generation of active species for the degradation of phenol:

I. The amorphous carbonate doping modifies the electronic band structure of TiO_2 by the strong electron-withdrawing bidentate carboxylate linkage, resulting in the formation of VB tail states and bandgap narrowing. Upon visible-light irradiation, electrons can be excited directly into the TiO_2 conduction band and are transferred to the adsorbed oxygen molecule to produce •O_2^- and subsequently the strongly oxidizing •OH. Meanwhile, the photogenerated hole will oxidize the adsorbed water molecule
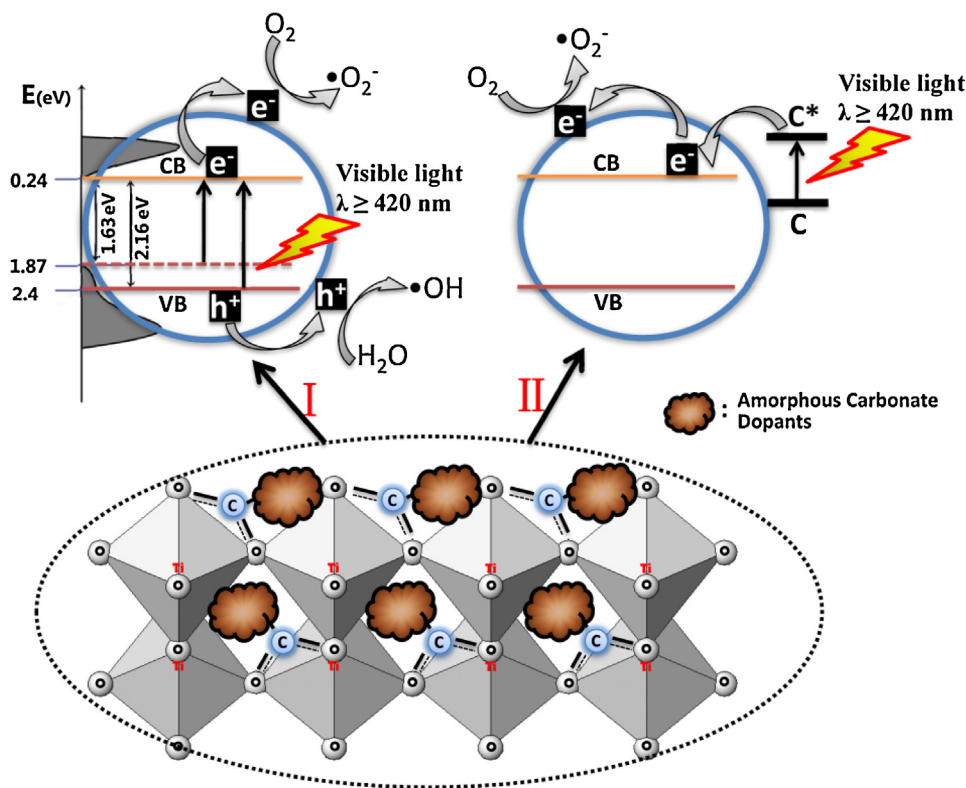
Fig. 8. Schematic illustrations for the proposed band structure of CT-300 and visible-light photocatalytic process.

to produce the $^\bullet$OH radical as well. The attached phenol can thus be attacked by $^\bullet$OH radicals. In addition to narrowing the bandgap, the carbonate dopants can help of enhancing the charge carrier separation through cooperation with bulk/surface defects of TiO_2, as discussed in the PL section.

II. It has been reported that visible-light photocatalytic activity can be enhanced by the carbonate species sensitized TiO_2. The carboxylate ligands enable good electronic communication between the photosensitizer and TiO_2 by forming a strong linkage with the TiO_2 surface [68]. Therefore, the carbonate species on the surface of TiO_2 can serve as a photosensitizer for absorption of visible light and inject electrons into the conduction band of TiO_2 through the bidentate carboxylate linkage. The injected electrons can be transferred to the adsorbed oxygen molecule to produce $^\bullet O_2{}^-$ and subsequently $^\bullet$OH, and then trigger the subsequent redox reactions similar to pathway I. The photosensitization of the carbonate dopants and the electron injection process from the photoexcited surface carbonate photosensitizer to the conduction band of the TiO_2 was demonstrated by the PL emission spectroscopy analyses and a parallel carbonate species sensitizing experiment (details can be found in Supplementary Material, Fig. S8).

For the two pathways, a greater number of hydroxyl radicals are expected to be generated in CT-300 to yield improved visible-light photocatalytic performance in comparison to other samples. The formation of photoinduced hydroxyl radicals is identified by photoluminescence technique using coumarin as a probe molecule, which readily reacted with $^\bullet$OH radical to produce highly fluorescent product, 7-hydroxycoumarin [69]. Fig. 9 shows the PL spectra and the PL intensity at 450 nm of 7-hydroxycoumarin against the irradiation time in the presence of CT-300. It can be seen that the generation of fluorescent 7-hydroxycoumarin is linearly proportional to irradiation time, confirming the rapid generation of
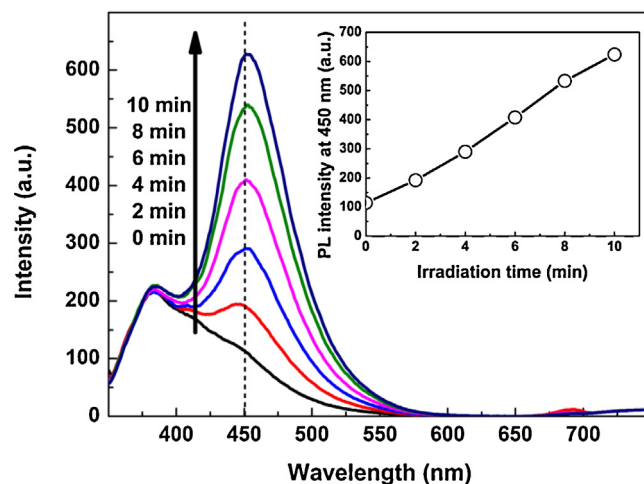

Fig. 9. Photoluminescence spectra of 7-hydroxycoumarin as a function of reaction times using CT-300 as the photocatalyst. The PL intensity at 450 nm of 7-hydroxycoumarin against the irradiation time is shown in the inset.

photoinduced hydroxyl radicals on CT-300 under visible-light irradiation ($\lambda \geq 420$ nm).

4. Conclusions

Carbonate-doped anatase TiO_2 photocatalysts have been successfully synthesized by combining a facile sol-gel method and a xerogel carbonization in hypoxic atmosphere. AcOH was used as the hydrolysis inhibitors of TBOT and the carbon source was the organic species produced during the synthesis of TiO_2 particles. The level of carbonate doping depends on the carbonization temperature. The carbonate dopants in TiO_2 lattice are found to exist at interstitial and/or surface positions with an amorphous

structure, which can narrow the TiO$_2$ bandgap effectively. For a sufficiently low carbonization temperature ($\leq$300 °C), the carboxylate ligands derived from the chelated AcOH molecules can be retained and transformed into the bidentate carboxylate linkage between the amorphous carbonate dopants and TiO$_2$ lattice. The strong electron-withdrawing bidentate carboxylate ligands can induce VB tail states to further narrow the TiO$_2$ bandgap. Moreover, the carbonate dopants can help promote the charge carriers' separation and serve as the photosensitizer for the absorption of visible light. The synergistic effects can significantly enhance the visible-light photocatalytic activities of TiO$_2$ for phenol degradation. The findings of our study may provide new insights for directing the design of new TiO$_2$-based photocatalysts without any complicated and expensive modification.

Acknowledgments

Appendix A. Supplementary data

Supplementary data associated with this article can be found, in the online version, at http://dx.doi.org/10.1016/j.apcatb.2016.09.057.

References

[1] B. Ohtani, J. Photochem. Photobiol. C: Photochem. Rev. 11 (2010) 157–178.
[2] K. Nakata, A. Fujishima, J. Photochem. Photobiol. C: Photochem. Rev. 13 (2012) 169–189.
[3] X.B. Chen, A. Selloni, Chem. Rev. 114 (2014) 9281±.
[4] M. Cargnello, T.R. Gordon, C.B. Murray, Chem. Rev. 114 (2014) 9319–9345.
[5] H. Xu, S. Ouyang, L. Liu, P. Reunchan, N. Umezawa, J. Ye, J. Mater. Chem. A 2 (2014) 12642–12661.
[6] J. Schneider, M. Matsuoka, M. Takeuchi, J.L. Zhang, Y. Horiuchi, M. Anpo, D.W. Bahnemann, Chem. Rev. 114 (2014) 9919–9986.
[7] B. Liu, L.M. Liu, X.F. Lang, H.Y. Wang, X.W. Lou, E.S. Aydil, Energy Environ. Sci. 7 (2014) 2592–2597.
[8] S. Wang, L. Zhao, L.N. Bai, J.M. Yan, Q. Jiang, J.S. Lian, J. Mater. Chem. A 2 (2014) 7439–7445.
[9] S. Yu, H.J. Yun, Y.H. Kim, J. Yi, Appl. Catal. B: Environ. 144 (2014) 893–899.
[10] Y.J. Yang, D.W. Ni, Y. Yao, Y.T. Zhong, Y. Ma, J.N. Yao, RSC Adv. 5 (2015) 93635–93643.
[11] Y. Zhang, Z. Zhao, J. Chen, L. Cheng, J. Chang, W. Sheng, C. Hu, S. Cao, Appl. Catal. B: Environ. 165 (2015) 715–722.
[12] F.L. Liu, X.D. Yan, X.J. Chen, L.H. Tian, Q.H. Xia, X.B. Chen, Catal. Today 264 (2016) 243–249.
[13] C. Lettmann, K. Hildenbrand, H. Kisch, W. Macyk, W.F. Maier, Appl. Catal. B: Environ. 32 (2001) 215–227.
[14] Q. Li, R. Xie, Y.W. Li, E.A. Mintz, J.K. Shang, Environ. Sci. Technol. 41 (2007) 5050–5056.
[15] P. Górska, A. Zaleska, E. Kowalska, T. Klimczuk, J.W. Sobczak, E. Skwarek, W. Janusz, J. Hupka, Appl. Catal. B: Environ. 84 (2008) 440–447.
[16] P. Wang, T. Zhou, R. Wang, T.-T. Lim, Water Res. 45 (2011) 5015–5026.
[17] P. Ganesan, A. Yella, T.W. Holcombe, P. Gao, R. Rajalingam, S.A. Al-Muhtaseb, M. Grätzel, M.K. Nazeeruddin, ACS Sustainable Chem. Eng. 3 (2015) 2389–2396.
[18] L. Zhang, J.M. Cole, ACS Appl. Mater. Interfaces 7 (2015) 3427–3455.
[19] R. Su, R. Tiruvalam, Q. He, N. Dimitratos, L. Kesavan, C. Hammond, J.A. Lopez-Sanchez, R. Bechstein, C.J. Kiely, G.J. Hutchings, F. Besenbacher, ACS Nano 6 (2012) 6284–6292.
[20] R. Parra, M.S. Góes, M.S. Castro, E. Longo, P.R. Bueno, J.A. Varela, Chem. Mater. 20 (2008) 143–150.
[21] S. Okunaka, H. Tokudome, Y. Hitomi, R. Abe, J. Mater. Chem. A 3 (2015) 1688–1695.
[22] J. Ye, W. Liu, J. Cai, S. Chen, X. Zhao, H. Zhou, L. Qi, J. Am. Chem. Soc. 133 (2011) 933–940.
[23] T. Ohsaka, F. Izumi, Y. Fujiki, J. Raman Spectrosc. 7 (1978) 321–324.
[24] L. Zhang, M.S. Tse, O.K. Tan, Y.X. Wang, M. Han, J. Mater. Chem. A 1 (2013) 4497–4507.
[25] L.-W. Zhang, H.-B. Fu, Y.-F. Zhu, Adv. Funct. Mater. 18 (2008) 2180–2189.
[26] P. Zhang, C. Shao, Z. Zhang, M. Zhang, J. Mu, Z. Guo, Y. Sun, Y. Liu, J. Mater. Chem. 21 (2011) 17746–17753.
[27] I. Luciu, R. Bartali, N. Laidani, J. Phys. D: Appl. Phys. 45 (2012) 345302.
[28] D.N. Voylov, A.L. Agapov, A.P. Sokolov, Y.M. Shulga, A.A. Arbuzov, Carbon 69 (2014) 563–570.
[29] G. Fu, P. Zhou, M. Zhao, W. Zhu, S. Yan, T. Yu, Z. Zou, Dalton Trans. 44 (2015) 12812–12817.
[30] J. Zhong, F. Chen, J.L. Zhang, J. Phys. Chem. C 114 (2010) 933–939.
[31] J.M. Liu, Q.C. Zhang, J.C. Yang, H.Y. Ma, M.O. Tade, S.B. Wang, J. Liu, Chem. Commun. 50 (2014) 13971–13974.
[32] D. Zhao, C. Chen, Y. Wang, W. Ma, J. Zhao, T. Rajh, L. Zang, Environ. Sci. Technol. 42 (2008) 308–314.
[33] I.X. Green, W. Tang, M. Neurock, J.T. Yates, J. Am. Chem. Soc. 134 (2012) 13569–13572.
[34] C.-y. Wang, H. Groenzin, M.J. Shultz, J. Am. Chem. Soc. 127 (2005) 9736–9744.
[35] Q.Y. Qu, H.W. Geng, R.X. Peng, Q. Cui, X.H. Gu, F.Q. Li, M.T. Wang, Langmuir 26 (2010) 9539–9546.
[36] K.D. Dobson, A.J. McQuillan, Spectrochim. Acta Part A 55 (1999) 1395–1405.
[37] R. Urlaub, U. Posset, R. Thull, J. Non-Cryst. Solids 265 (2000) 276–284.
[38] J. Llorca, N. Homs, P.R. de la Piscina, J. Catal. 227 (2004) 556–560.
[39] V.A. Nadtochenko, A.G. Rincon, S.E. Stanca, J. Kiwi, J. Photochem. Photobiol. A: Chem. 169 (2005) 131–137.
[40] X. Wu, S. Yin, Q. Dong, C. Guo, H. Li, T. Kimura, T. Sato, Appl. Catal. B: Environ. 142–143 (2013) 450–457.
[41] S. Yu, S. Ahmadi, C. Sun, P. Palmgren, F. Hennies, M. Zuleta, M. Göthelid, J Phys. Chem. C 114 (2010) 2315–2320.
[42] J. Klein, E. Dunkelblum, D. Avrahami, J. Org. Chem. 32 (1967) 935–939.
[43] H. Mimoun, R. Charpentier, A. Mitschler, J. Fischer, R. Weiss, J. Am. Chem. Soc. 102 (1980) 1047–1054.
[44] S. Fujita, S. Steenken, J. Am. Chem. Soc. 103 (1981) 2540–2545.
[45] R.J. Waltman, A.F. Diaz, J. Bargon, J. Phys. Chem. 88 (1984) 4343–4346.
[46] J. Wang, X. Ni, J. Appl. Polym. Sci. 108 (2008) 3552–3558.
[47] K.E. Lee, M.A. Gomez, T. Regier, Y. Hu, G.P. Demopoulos, J. Phys. Chem. C 115 (2011) 5692–5707.
[48] W. Wei, C. Yu, Q. Zhao, G. Li, Y. Wan, Chem. Eur. J. 19 (2013) 566–577.
[49] X. Jiang, Y. Zhang, J. Jiang, Y. Rong, Y. Wang, Y. Wu, C. Pan, J. Phys. Chem. C 116 (2012) 22619–22624.
[50] P. Zhang, C. Shao, Z. Zhang, M. Zhang, J. Mu, Z. Guo, Y. Liu, Nanoscale 3 (2011) 2943–2949.
[51] L. Jing, B. Xin, F. Yuan, L. Xue, B. Wang, H. Fu, J. Phys. Chem. B 110 (2006) 17860–17865.
[52] K. Nagaveni, M.S. Hegde, N. Ravishankar, G.N. Subbanna, G. Madras, Langmuir 20 (2004) 2900–2907.
[53] D.-H. Wang, L. Jia, X.-L. Wu, L.-Q. Lu, A.-W. Xu, Nanoscale 4 (2012) 576–584.
[54] X.-b. Yan, B.K. Tay, Y. Yang, J. Phys. Chem. B 110 (2006) 25844–25849.
[55] S.-X. Liu, J.-L. Liu, X.-S. Li, X. Zhu, A.-M. Zhu, Plasma Process. Polym. 12 (2015) 422–430.
[56] Z. He, W. Que, Y. He, RSC Adv. 4 (2014) 3332–3339.
[57] X. Chen, C. Burda, J. Am. Chem. Soc. 130 (2008) 5018–5019.
[58] G. Liu, L. Wang, C. Sun, X. Yan, X. Wang, Z. Chen, S.C. Smith, H.-M. Cheng, G.Q. Lu, Chem. Mater. 21 (2009) 1266–1274.
[59] X. Chen, L. Liu, P.Y. Yu, S.S. Mao, Science 331 (2011) 746–750.
[60] D. Li, H. Haneda, S. Hishita, N. Ohashi, Chem. Mater. 17 (2005) 2596–2602.
[61] Z. Bian, J. Zhu, F. Cao, Y. Lu, H. Li, Chem. Commun. (2009) 3789–3791.
[62] Y.J. Yang, Y. Yao, L. He, Y.T. Zhong, Y. Ma, J.N. Yao, J. Mater. Chem. A 3 (2015) 10060–10068.
[63] M. Nasir, Z. Xi, M. Xing, J. Zhang, F. Chen, B. Tian, S. Bagwasi, J. Phys. Chem. C 117 (2013) 9520–9528.
[64] M. Kong, Y. Li, X. Chen, T. Tian, P. Fang, F. Zheng, X. Zhao, J. Am. Chem. Soc. 133 (2011) 16414–16417.
[65] T.L. Thompson, J.T. Yates, Chem. Rev. 106 (2006) 4428–4453.
[66] M.V. Dozzi, B. Ohtani, E. Selli, PCCP 13 (2011) 18217–18227.
[67] R. Quesada-Cabrera, A. Mills, C. O'Rourke, Appl. Catal. B: Environ. 150–151 (2014) 338–344.
[68] Y. Ooyama, S. Inoue, T. Nagano, K. Kushimoto, J. Ohshita, I. Imae, K. Komaguchi, Y. Harima, Angew. Chem Int. Ed. 50 (2011) 7429–7433.
[69] Z.a. Huang, Q. Sun, K. Lv, Z. Zhang, M. Li, B. Li, Appl. Catal. B: Environ. 164 (2015) 420–427.